Chemical Science

ROYAL SOCIETY OF CHEMISTRY

EDGE ARTICLE

View Article Online
View Journal | View Issue

Cite this: *Chem. Sci.*, 2024, **15**, 10491

All publication charges for this article have been paid for by the Royal Society of Chemistry

Synergistic *meso*-β regulation of porphyrins: squeezing the band gap into the near-infrared I/II region†

Chulin Qu, [a] Xinxin Gong,[a] Yufen Sun,[a] Hu Gao, [a] Fangjian Cai,[a] Yue Zhao, [a] Fan Wu *[ab] and Zhen Shen *[a]

Received 18th March 2024
Accepted 1st June 2024

DOI: 10.1039/d4sc01806k

rsc.li/chemical-science

The development of novel near-infrared (NIR) materials with extremely small energy gaps and high stability is highly desirable in bioimaging and phototherapy. Here we report an effective strategy for narrowing the energy gaps of porphyrins by synergistic regulation of *meso*/β substituents. The novel NIR absorbing/emitting *meso*-alkynyl naphthoporphyrins (**Zn-TNP** and **Pt-TNP**) are synthesized *via* the retro-Diels–Alder reaction. X-ray crystallography analysis confirms the highly distorted structures of the complexes. Both compounds exhibit intense Q bands around 800 nm, while **Zn-TNP** shows deep NIR fluorescence at 847 nm. **Pt-TNP** displays NIR-II room temperature phosphorescence peaking at 1106 nm with an extremely large Stokes shift of 314 nm, which are the longest wavelengths observed among the reported platinum porphyrinoids. Furthermore, **Pt-TNP** shows remarkable photostability and a notable capacity for synchronous singlet oxygen and heat generation under NIR light irradiation, demonstrating potential in combined photodynamic/photothermal therapy. A theoretical analysis reveals the progressive lifting of the HOMO by the β-fused benzene ring, the decrease of the LUMO upon *meso*-alkynyl substitution, and energy-releasing pathways varying with metal ions. This dual regulation approach demonstrates great promise in designing innovative multifunctional NIR porphyrin materials.

Introduction

Organic near-infrared (NIR) materials are in high demand for bio-imaging and phototherapy due to their great advantages including low cytotoxicity, deep tissue penetration, and minimal damage to normal tissues.[1–5] As important pigments of life, porphyrinoids can be readily functionalized *via* inner-core coordination and peripheral modifications. The common tetrapyrrolic porphyrins are 18π aromatic conjugated molecules displaying intense Soret bands and weak Q bands in the visible region, but they lack near-infrared (NIR) absorption. Therefore, considerable effort has been devoted to obtaining NIR-absorbed porphyrinoids by modifying the structure, which narrows the highest occupied molecular orbital (HOMO)–lowest unoccupied molecular orbital (LUMO) gap. Among various designing strategies, such as developing π-extended,[6] MO-mixing[7,8] and donor–acceptor[9] systems, pyrrolic β-aromatic-fusion[10] stands out as an exceptional approach for producing rigid porphyrins with intensified Q bands in NIR-absorption and emission. The Q bands of porphyrins can undergo a gradual red-shift by the tetra-fusion of benzene[11–13] (600–700 nm), naphthalene[14–16] (700–800 nm), and anthracene[17–20] (>800 nm), accompanied by a notable intensity increase.[21] Despite having the longest NIR absorption and emission bands, the anthracene-fused (anthro) porphyrins were easily photooxidized under ambient light,[22] which severely restricted their practical uses.

While considerable research has been conducted on expanding the porphyrinoid π-system *via* pyrrolic β-functionalization, little attention has been paid to decreasing the HOMO–LUMO gap by adjusting *meso*-substituents. Most porphyrins have *meso*-aryl substituents, resulting in a minor change in the HOMO–LUMO gap, because both electron-withdrawing and electron-donating groups in phenyl always cause a simultaneous rise or decrease in the HOMO and LUMO. Kobayashi *et al.* reported the design of stable, NIR-absorbing phthalocyanines by rationally controlling both the central core and the α-substituent, demonstrating the efficiency of multipart regulation in energy-gap tuning.[23–25] *Meso*-alkynyl groups have been incorporated into porphyrinoids[26] to facilitate intermolecular coupling and create nanoscale tape and rings[27–29] with a high degree of conjugation. In this work, combined with π-extension at β-positions, we highlight the additional HOMO–

[a]*State Key Laboratory of Coordination Chemistry, Collaborative Innovation Center of Advanced Microstructures, School of Chemistry and Chemical Engineering, Nanjing University, Nanjing 210023, China. E-mail: wufan@nnu.edu.cn; zshen@nju.edu.cn*

[b]*School of Chemistry and Materials Science, Nanjing Normal University, Nanjing 210023, China*

† Electronic supplementary information (ESI) available: Materials and methods, characterization, additional spectroscopic data, theoretical analysis, X-ray crystallographic data, and simulation of magnetically induced ring currents. CCDC 2325275 and 2265412. For ESI and crystallographic data in CIF or other electronic format see DOI: https://doi.org/10.1039/d4sc01806k

LUMO gap narrowing ability of alkynyl groups at *meso* positions (Fig. 1). Upon the *meso*-β double regulation, our newly synthesized *meso*-alkynyl naphthalene-fused (naphtho)porphyrin complexes **Zn-TNP** and **Pt-TNP** demonstrate not only a more pronounced red-shift in both absorption and emission (>800 nm), but also significantly higher photostability than their NIR-absorbing *meso*-aryl anthroporphyrin counterparts. Notably, the platinum coordinated **Pt-TNP** is a rare example of a porphyrinoid emitter that displays phosphorescence in the desirable NIR-II (1000–1400 nm) window with a maximum of 1106 nm at room temperature, while presenting an ultra-large Stokes shift exceeding 300 nm. Furthermore, **Pt-TNP** exhibits significant singlet oxygen generation and photothermal conversion capacity under NIR laser irradiation, making it an ideal agent for multifunctional phototherapy.[30]

Results and discussion

The synthesis route is presented in Fig. 2a. 4,9-Dihydro-4,9-ethano-2*H*-benz[*f*]isoindole **1** bearing a bicyclo[2.2.2]octadiene (BCOD) unit was synthesized *via* a reported method.[31] The condensation of **1** and 3-(triisopropylsilyl)propiolaldehyde **2** (ref. [32]) was catalyzed by $BF_3{\cdot}OEt_2$ in ultra-dry CH_2Cl_2 under an N_2 atmosphere, followed by oxidation with *p*-chloranil (TCQ), and afforded free-base porphyrin **3** in 9% yield.[33] Adding a methanol solution of $Zn(OAc)_2$ to the $CHCl_3$ solution of **3** afforded the zinc-coordinated porphyrin **Zn-3** in 93% yield. The platinum complex **Pt-3** was synthesized in 93% yield *via* the reaction between **3** and $PtCl_2$ in refluxing acetic acid. The naphthoporphyrins **Zn-TNP** and **Pt-TNP** were quantitatively obtained by employing the retro-Diels–Alder method,[34] heating precursors **Zn-3** and **Pt-3** in solid states, respectively, at 300 °C under vacuum.

The successful synthesis of the desired fused porphyrins was confirmed by HR-ESI mass spectrometry and MALDI-TOF mass spectrometry (Fig. S1–S10†), and nuclear magnetic resonance (NMR) spectroscopy (Fig. S12–S16†). The resonance signals of protons on the fused naphthalenes of **Zn-TNP** (Fig. 2b) are divided into three groups: H_1 at δ = 10.9 ppm, H_2 at δ = 8.41 ppm and H_3 at δ = 7.75 ppm, which shift more downfield than those of the *meso*-tetraphenyl[2,3]tetranaphthoporphyrin zinc complex (**Zn-TPTNP**) reported by Ito *et al.*[14,35] The NMR computational simulation of **Zn-TNP** shows consistency with the experimental results, with H_1 at δ = 10.9/11.0 ppm, H_2 at δ = 8.56/8.66 ppm, and H_3 at δ = 7.95/7.97 ppm. To further explain the downfield proton signals on **Zn-TNP**, particularly the significantly shifted H_1, the 3D isochemical shielding surface (ICSS) calculation[36,37] was performed (Fig. 2c). The overall aromaticity of **Zn-TNP** is indicated by the large shielding area (blue) enclosing the entire molecule. Enhanced deshielding (red) is observed in the area between the alkynyl groups and fused naphthalenes of **Zn-TNP**, which mainly surrounds the H_1 protons. Consequently, the presence of alkynyl groups induces a more significant downfield shift in the signal of H_1, while the signals of H_2 and H_3 also undergo a slight downfield shift.

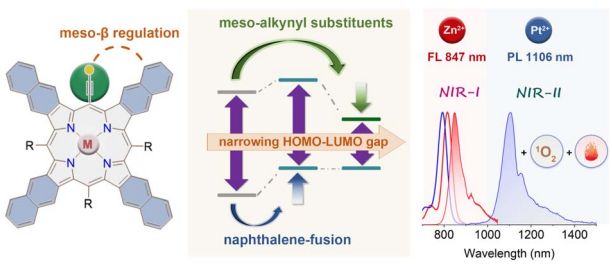

Fig. 1 Molecular design of target NIR-absorbing/emitting porphyrin complexes.

The solid structures of **Zn-TNP** and **Pt-TNP** were examined using single-crystal X-ray diffraction. The single crystals of **Zn-TNP** were obtained by slow diffusion of hexane into its CH_2Cl_2 solution containing a small amount of Et_4NCl. As a consequence of Cl^- axial coordination, the Zn–N bond lengths range from 2.072(5) to 2.137(6) Å, which are longer than those of common four-coordinated Zn porphyrins (2.039–2.040 Å).[38] The Zn(II) ion is located at 0.384 Å above the 4N plane, and the length of the Zn–Cl bond is 2.335(2) Å. The single crystals of **Pt-TNP** were obtained by slow evaporation of its toluene solution for a month. The bond length of Pt–N is 2.0073(14) Å, which is identical to those of the reported (5,10,15,20-tetraphenyl-21*H*,23*H*-porphinato)platinum(II).[39] The bond length alternations in crystal structures are analyzed by the harmonic oscillator model of aromaticity[40] (HOMA). The HOMA values of **Zn-TNP** and **Pt-TNP** for the 18π-circuit (containing 16 atoms as a macrocyclic internal cross) are 0.88 and 0.90, respectively, which are typical for aromatic porphyrinoids.[41] **Zn-TNP** and **Pt-TNP** have skeleton lengths of 16.957 Å and 17.179 Å, respectively, determined by the distance between the terminal carbon atoms on the fused naphthalenes (Fig. 3a). Both **Zn-TNP** and **Pt-TNP** exhibit highly distorted conformations, which are further investigated using the clothes-line diagrams (Fig. 3b) and normal-coordinate structural decomposition (NSD) method[42,43] (Tables S3 and S4†). **Zn-TNP** has a saddled conformation (B_{2u} = 1.89), while **Pt-TNP** has a distinct hybrid conformation that is primarily saddled (B_{2u} = 2.59) and partly ruffled (B_{1u} = 1.15). The single crystal packing structure of **Zn-TNP** displays a wave-shaped extension along the *a* and *c* directions. The formation of the "wave" is constructed by the face-to-face π-stacking between the fused naphthalenes in **Zn-TNP** molecules. And the **Zn-TNP** wave layers are separated by the Et_4N^+ counterions. The packing structure of **Pt-TNP** is arranged in an interleaved manner, showing slipped π–π interaction of the fused naphthalenes (Fig. 3c).

The absorption, luminescence, and magnetic circular dichroism (MCD) spectra of the new porphyrin compounds were recorded in toluene to investigate the photophysical properties (Fig. 4a and b). The precursors **Zn-3** and **Pt-3** display typical intense Soret bands at 487 and 466 nm, respectively, which are red-shifted in comparison to the Soret band of *meso*-tetraphenylporphyrin at *ca.* 410 nm (Fig. S21 and S22†). The Soret bands of **Zn-TNP** and **Pt-TNP** are further red-shifted to 549 nm and 520 nm, respectively. The Q bands of the **Zn-3** and **Pt-3** are weak and located in the visible region. After naphthalene-fusion, the Q bands of **Zn-TNP** and **Pt-TNP**

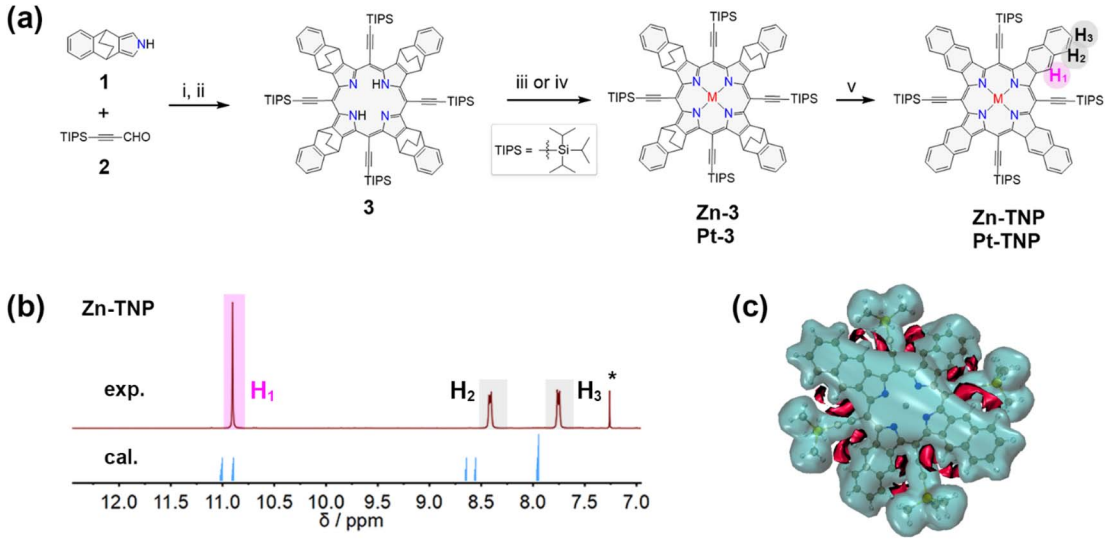

Fig. 2 (a) Synthesis of BCOD and π-extended porphyrins: (i) $BF_3{\cdot}OEt_2$, CH_2Cl_2, −78 °C, 2 h; (ii) TCQ, r.t., 30 min; (iii) $Zn(OAc)_2{\cdot}2H_2O$, $CHCl_3$/MeOH, r.t., 3 h; (iv) $PtCl_2$, NaOAc, AcOH, 118 °C, N_2, 24 h; (v) 300 °C, 30 min, *in vacuo*. (b) ^1H NMR spectra of **Zn-TNP**: experimental data (above) measured in $CDCl_3$ and simulated data (below). (c) 3D ICSS map of **Zn-TNP** (isovalue = 1.5). The shielding areas are transparent blue and deshielding areas are solid red.

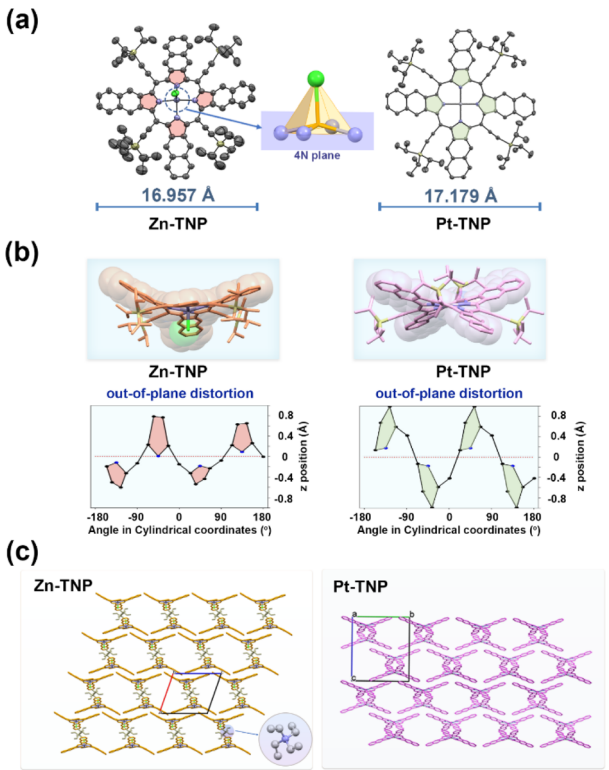

Fig. 3 (a) Top views of single crystal structures of **Zn-TNP** and **Pt-TNP** using an ORTEP diagram with thermal ellipsoids drawn at the 50% probability. (b) Side views and out-of-plane distortions of **Zn-TNP** and **Pt-TNP**. (c) Packing diagrams of **Zn-TNP** and **Pt-TNP**. In the packing views, *meso*-substituents are omitted for clarity.

significantly strengthen with more than 3-fold intensity and shift to the NIR region, peaking at 816 and 792 nm, respectively. The MCD spectrum of **Zn-TNP** shows derivative-shaped Faraday A_1 terms with a pair of opposite signs at the absorption of B_{00} (549 nm) and Q_{00} (816 nm), respectively, indicating the presence of a highly symmetrical structure and degenerate excited states.[44] The Faraday A_1 terms of **Zn-TNP** show a negative-to-positive sign sequence in ascending energy, indicating that the energy difference between HOMO and HOMO−1 (ΔHOMO) is larger than that between LUMO and LUMO+1 (ΔLUMO).[45] The MCD pattern of **Pt-TNP** is identical to that of **Zn-TNP**. Compounds **3** and **Zn-3** show fluorescence bands at 742 nm and 679 nm (Fig. S25 and S26†), respectively, while **Zn-TNP** shows a red-shifted fluorescence band at 847 nm (Fig. 4b, purple line). The Pt complexes exhibit room temperature phosphorescence (RTP). **Pt-3** shows phosphorescence emission at 823 nm with a shoulder at 930 nm (Fig. S27†). For **Pt-TNP**, the RTP was detected in the range from 1000 to 1400 nm in deaerated toluene, showing the maximum at 1106 nm (Fig. 4b, red line). The phosphorescence band of **Pt-TNP** is located in the NIR-II region and more red-shifted than that of any other reported Pt-coordinated porphyrins.[21,46] Moreover, **Pt-TNP** has a very large Stokes shift of 314 nm, making it a potential NIR-II phosphorescence probe for biomedical imaging. In air-saturated toluene, the RTP of **Pt-TNP** could also be observed with reduced intensity, and the singlet oxygen ($^1O_2$) generation capacity of **Pt-TNP** was revealed by the finding of a $^1O_2$ phosphorescence peak at 1270 nm (Fig. 4c, black line). The $^1O_2$ generation abilities of **Pt-TNP** and **Zn-TNP** were compared utilizing 1,3-diphenylisobenzofuran (DPBF) as a singlet oxygen scavenger (Fig. 4d, S34 and S35†). Under laser irradiation (808 nm, 10 mW cm^{-2}), the absorbance of DPBF in toluene exhibited no significant change without the addition of porphyrin compounds, but decreased significantly in 21 s with the presence of **Pt-TNP**. Furthermore, **Pt-TNP** exhibited excellent photostability, whereas **Zn-TNP** was unstable under

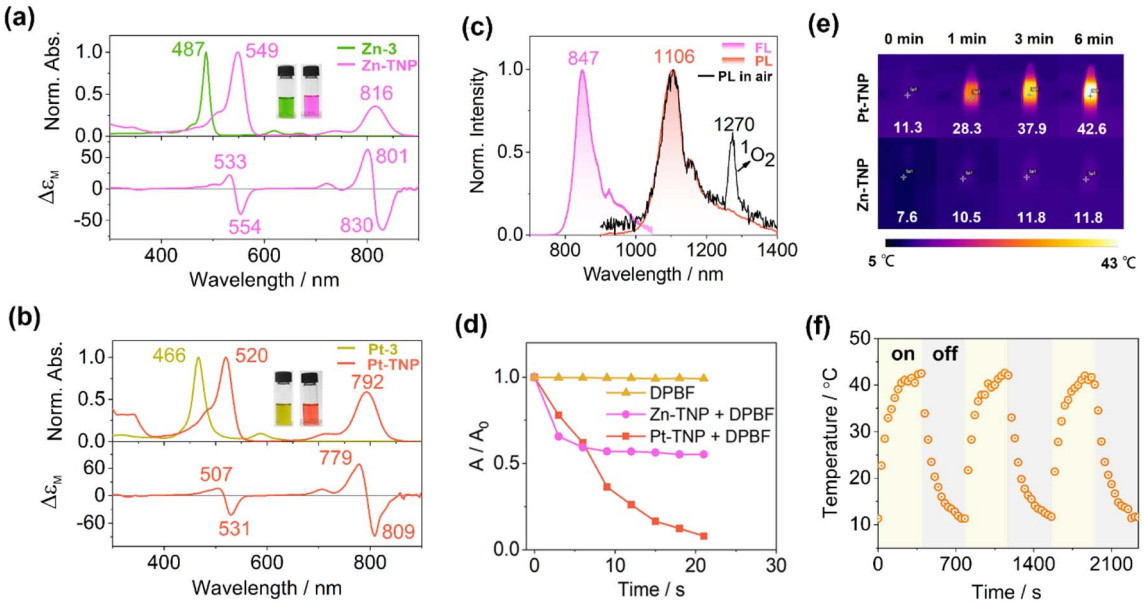

Fig. 4 (a and b) Absorption spectra of **Zn-3**, **Zn-TNP**, **Pt-3** and **Pt-TNP** in toluene, and the MCD spectra of **Zn-TNP** and **Pt-TNP** in toluene. Inset: solution photographs of **Zn-3**, **Zn-TNP**, **Pt-3**, and **Pt-TNP**. (c) Fluorescence spectrum of **Zn-TNP** (λ_{ex} = 549 nm, purple line) in toluene, and phosphorescence spectra of **Pt-TNP** in deaerated and air-saturated toluene (λ_{ex} = 520 nm, red line and black line). (d) The absorption changes at 415 nm of DPBF, **Zn-TNP** + DPBF, and **Pt-TNP** + DPBF in toluene under 808 nm (10 mW cm^{-2}) laser irradiation within 21 s. (e) Thermal images of **Pt-TNP** and **Zn-TNP** (30 μmol) under 808 nm laser irradiation (0.35 W cm^{-2}). (f) Heating–cooling cycles for **Pt-TNP** (30 μmol) under 808 nm laser irradiation (0.35 W cm^{-2}).

irradiation and underwent rapid photobleaching (Fig. 4d and S36†). Previous research has demonstrated that zinc porphyrins can undergo photo-oxidation upon light exposure.[47,48] The easier photodegradation of **Zn-TNP** may be attributed to its better oxygen affinity than **Pt-TNP** (Fig. S11, S18 and S19†), while the detailed mechanism still requires further investigation.[49,50] The photothermal conversion performance of **Pt-TNP** and **Zn-TNP** was investigated in toluene under 808 nm (0.35 W cm^{-2}) laser irradiation. After 6 minutes of irradiation, the **Pt-TNP** solution had a temperature increase of over 30 °C, whereas the **Zn-TNP** solution only increased by around 4 °C due to photoinstability (Fig. 4e and S33†). The heating–cooling measurements of **Pt-TNP** demonstrated excellent repeatability after three cycles (Fig. 4f and S30†). A time constant (τ) of 120.05 was obtained by linearly fitting time (t) as a function of the negative natural logarithm of the driving force temperature ($-\ln\theta$) at the cooling stage (Fig. S32†). The calculated photothermal conversion efficiency for the **Pt-TNP** solution was 78%.

DFT calculations were performed on a series of Pt porphyrins to evaluate the effects of *meso*- and β-substituents on their energy gaps (Fig. 5a and S39†). The *meso*-phenyl, β-non-fused (N = 0) platinum porphyrin **Pt-TPP** has degenerate LUMO/LUMO+1 and near-degenerate HOMO/HOMO−1, showing a large HOMO–LUMO gap of 3.05 eV. The naphthalene-fusion (N = 2) of **Pt-TPP** considerably lifts its a_{1u}-type HOMO−1 but has little effect on the a_{2u}-type HOMO, resulting in a HOMO/LUMO switch and a huge HOMO/HOMO−1 splitting with a largely reduced HOMO–LUMO gap of 2.24 eV in **Pt-TPTNP** (Fig. S48†). By replacing the phenyl group with either the electron-withdrawing pentafluorophenyl group or the electron-donating 4-*N*,*N*-dimethylphenyl group, the naphthoporphyrin undergoes a simultaneous increase or decrease in both HOMO and LUMO energy levels, resulting in a very small change of the HOMO–LUMO gap. In contrast, the *meso*-alkynyl **Pt-TNP** (where triisopropylsilylethynyl is replaced by trimethylsilylethynyl) exhibits not only a significantly elevated HOMO consistent with its *meso*-phenyl counterpart, but also a substantially reduced LUMO due to the presence of electron-withdrawing alkynyl groups. The *meso*-β double regulation of **Pt-TNP** efficiently reduces the HOMO–LUMO gap to 1.92 eV, with the electron density extending to the fused naphthalenes on the HOMO and *meso*-alkynyl groups on the LUMO. It is noteworthy that the extended electron-density distributions towards alkynyl groups are exclusively observed in the LUMOs, but not in the HOMOs; therefore, conjugative extension could potentially play a substantial role in the large energy decreases of the LUMOs. Additional computational analysis reveals that replacing trimethylsilyl groups with H has a negligible impact on the HOMO/LUMO energy levels. By introducing electron-withdrawing groups like –CF_3 and –CN into the alkynyl groups, the HOMO–LUMO gaps are further reduced to 1.80 eV and 1.66 eV, respectively (Fig. S40†). This energy-gap decrease is accompanied by a further extension of the electron density towards the terminal group.

The optimized structures of **Pt-TNP** and **Zn-TNP** are distorted, but they exhibit varying degrees and patterns of distortion compared to the single-crystal structures (Fig. S53†). These distortions may be caused by steric effects and further influenced by the crystal-packing forces. We successfully optimized **Zn-TNP** for both saddled (***sad*-Zn-TNP**) and ruffled (***ruf*-Zn-TNP**)

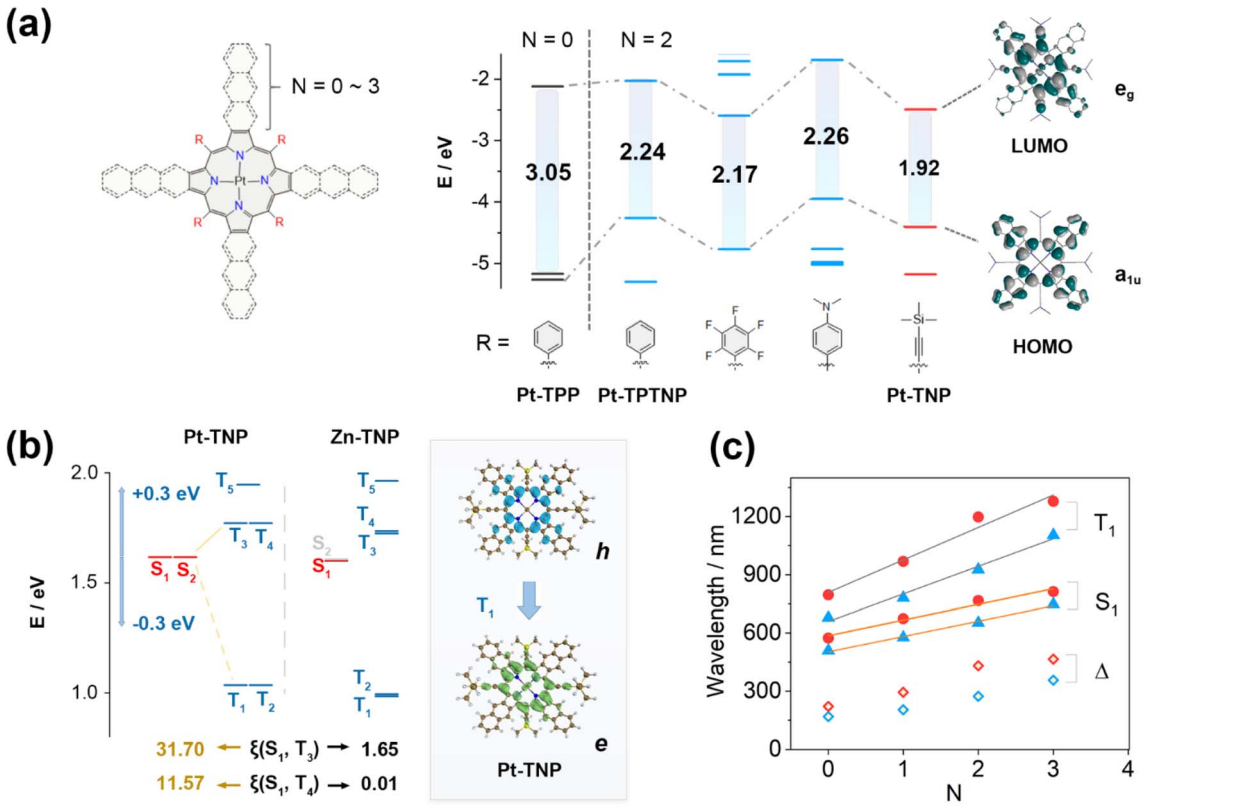

Fig. 5 (a) Frontier molecular orbital diagrams of **Pt-TNP** and other Pt–porphyrins for comparison. (b) Schematic diagram of the calculated energy gaps, spin–orbit coupling constants between S_1 and T_n ($n = 3$–4) of **Pt-TNP** and **Zn-TNP**, and the hole and electron distribution in the S_0–T_1 transition of **Pt-TNP**. (c) Plots of absorption and phosphorescence peaks of *meso*-phenyl (blue triangle) and *meso*-alkynyl (red circle) Pt–porphyrins *versus* linearly fused benzene numbers (*N*) in β positions ranging from 0 to 3. Stokes shifts are presented as blue and red rhombuses.

conformations. The total energies, HOMO–LUMO energy levels, and energy gaps of ***sad*-Zn-TNP** and ***ruf*-Zn-TNP** are nearly identical, suggesting that the distortion patterns have minimal impact on the electronic structures and optical properties. DFT calculations are also conducted on a variety of *meso*-free/β-fused and β-free/*meso*-substituted porphyrins, all of which exhibit completely planar conformations due to reduced steric hindrance. The significant HOMO-lifting effect of aromatic fusion and the LUMO-reducing effect of alkynyl substitution, which can be controlled by the degree of π-extension, were further validated on the planar porphyrin molecules (Fig. S38†).

Time-dependent (TD) DFT calculations were performed to further investigate the influence of excited states caused by different substituents and coordinated metal ions (Fig. 5b and c). The energy levels of the S_1 and T_n states of **Pt-TNP** and **Zn-TNP** are similar, and both compounds exhibit degenerate S_1/S_2 and T_1/T_2 states. **Zn-TNP** and **Pt-TNP** have large S_1–T_1 gaps ($\Delta E_{S_1-T_1}$) of 0.62 eV and 0.58 eV, respectively, while their T_3 and T_4 states have small S_1–T_n gaps ($\Delta E_{S_1-T_n}$ < 0.3 eV),[51] which promote the intersystem crossing (ISC) activities. The S_1–T_n spin–orbit coupling matrix elements (SOCMEs) of **Zn-TNP** are smaller than 2.4 cm^{-1}. In contrast, the S_1–T_3 and S_1–T_4 SOCMEs for **Pt-TNP** have large values of 31.70 and 11.57 cm^{-1}, respectively. The energy can efficiently pass through the ISC process between S_1 and T_3 of **Pt-TNP** due to the narrow energy gap ($\Delta E_{S_1-T_3}$ = 0.15 eV) and large SOCME. Subsequently, the energy undergoes a rapid internal conversion (IC) to T_1 and deactivates to the ground state S_0 with phosphorescence emission. The T_1 state of **Pt-TNP** can react with oxygen to generate singlet oxygen, and a significant amount of energy can be released as heat through internal conversion. The electron and hole distributions of **Pt-TNP** indicate that both S_0–S_1 and S_0–T_1 are π–π* transitions with negligible involvement of a central metal (Fig. 5b and S75†). The Sr index, which indicates the degree of electron–hole overlap, is 0.86 for S_1 and 0.79 for T_1, demonstrating that the two states are locally excited (LE).

The wavelength variation trends for the longest absorption (S_0–S_1) and phosphorescence (S_0–T_1) peaks of a series of Pt porphyrins are investigated (Fig. 5c). The molecules are divided into two groups: *meso*-phenyl (blue triangle) and *meso*-alkynyl (red circle). Each group contains four molecules, with the number of linearly fused benzenes (*N*) ranging from 0 to 3. In both groups, the calculated wavelengths corresponding to S_1, T_1, and Stokes shifts increase as *N* increases, and the wavelengths in the *meso*-alkynyl group are always larger than those in the *meso*-phenyl group with the same *N* value. The plots of the S_1 and T_1 wavelengths as a function of *N* exhibit strong linear correlations in both groups, with the slopes of the fitting lines for T_1 being larger than those for S_1. The *meso*-alkynyl group with a larger *N* yields greater calculated Stokes shifts, which is consistent with the remarkably large experimental Stokes shift of **Pt-TNP** (314 nm) resulting from the *meso*-β double regulation.

Based on the optimized structure of **Pt-TNP** and **Zn-TNP**, we evaluated the ring currents and induced magnetic shielding with a nucleus-independent chemical shift[52] (NICS), anisotropy of the induced current density[53] (ACID), and the gauge-including magnetically induced current[54,55] (GIMIC) calculations (Table S7 and Fig. S76–S78†). The NICS(0) values are negative in both the fused naphthene and porphyrin core for both compounds. The diatropic ring currents of **Zn-TNP** and **Pt-TNP** continuously flow throughout the whole structure, showing the global aromaticity of these two compounds. Additionally, localized diatropic ring currents are observed on the naphthalene moieties and the inner 16-bond porphyrin core.

Conclusions

In summary, we successfully synthesized porphyrin complexes with remarkable red-shifted NIR absorption and emission (ranging from 800 to 1200 nm) by tailoring the molecular energy levels through *meso*- and β-substituents. The electronic structures and optical properties of target *meso*-alkynyl naphthoporphyrin complexes **Zn-TNP** and **Pt-TNP** were fully elucidated *via* spectroscopic measurements and theoretical calculations. The solid structures of the complexes were analyzed using single-crystal X-ray diffraction, revealing saddling or mixed saddling–ruffling distortions. **Zn-TNP** and **Pt-TNP** displayed Q bands at 816 nm and 792 nm, respectively. **Zn-TNP** exhibited a fluorescence band at a wavelength of 847 nm. **Pt-TNP** exhibited room-temperature NIR-II phosphorescence at 1106 nm with a huge Stokes shift, and its ability to produce singlet oxygen was directly shown by the emission at 1270 nm. **Pt-TNP** also demonstrated excellent NIR photothermal conversion capacity. The dual functionality of **Pt-TNP** in singlet oxygen and heat generation makes it a promising candidate for combined photothermal/photodynamic therapy. While aromatic-ring-fusion is a well-established approach for reducing the HOMO–LUMO gap by HOMO-lifting, the additional functionalization of alkynyl groups in *meso* positions causes more than 100 nm of shifting in absorption/emission bands by LUMO-reduction when compared to their aryl-substituted counterparts. The DFT calculations provided an in-depth explanation of the correlation between the decrease in S_1/T_1 energy levels and the incorporation of *meso*-β substituents, as well as enhanced ISC activity in the Pt complex. The *meso*-β dual regulation of porphyrins effectively reduces the energy gap and modulates the excited states, offering a promising strategy for developing novel stable NIR materials.

Data availability

All experimental details including synthetic procedures, spectroscopic data, and theoretical calculation results, are available in the ESI.†

Author contributions

C. Q. carried out the synthesis, characterization, manuscript writing and theoretical calculations. X. G., Y. S., H. G. and F. C. contributed to the synthesis, characterization, and data analysis. C. Q., H. G. and Y. Z. performed the single-crystal X-ray diffraction measurements and analysis. F. W. and Z. S. designed and supervised the project, and revised the manuscript. All authors discussed the results and commented on the manuscript.

Conflicts of interest

There are no conflicts to declare.

Acknowledgements

This work was supported by the National Natural Science Foundation of China (Grants 22271140, 22071103, and 22371118). The theoretical calculations are performed using the supercomputing resources at the High-Performance Computing Center of Nanjing University.

Notes and references

1 F. Ding, Y. Zhan, X. Lu and Y. Sun, Recent advances in near-infrared II fluorophores for multifunctional biomedical imaging, *Chem. Sci.*, 2018, **9**, 4370–4380.
2 S. He, J. Song, J. Qu and Z. Cheng, Crucial breakthrough of second near-infrared biological window fluorophores: design and synthesis toward multimodal imaging and theranostics, *Chem. Soc. Rev.*, 2018, **47**, 4258–4278.
3 G. Hong, A. L. Antaris and H. Dai, Near-infrared fluorophores for biomedical imaging, *Nat. Biomed. Eng.*, 2017, **1**, 0010.
4 L. Li, X. Han, M. Wang, C. Li, T. Jia and X. Zhao, Recent advances in the development of near-infrared organic photothermal agents, *Chem. Eng. J.*, 2021, **417**, 128844.
5 V.-N. Nguyen, Z. Zhao, B. Z. Tang and J. Yoon, Organic photosensitizers for antimicrobial phototherapy, *Chem. Soc. Rev.*, 2022, **51**, 3324–3340.
6 G. Anguera, W.-Y. Cha, M. D. Moore, J. Lee, S. Guo, V. M. Lynch, D. Kim and J. L. Sessler, Hexadecaphyrin-(1.0.0.0.1.1.0.1.1.0.0.0.1.1.0.1): A Dual Site Ligand That Supports Thermal Conformational Changes, *J. Am. Chem. Soc.*, 2018, **140**, 4028–4034.
7 Y. Wang, H. Kai, M. Ishida, S. Gokulnath, S. Mori, T. Murayama, A. Muranaka, M. Uchiyama, Y. Yasutake, S. Fukatsu, Y. Notsuka, Y. Yamaoka, M. Hanafusa, M. Yoshizawa, G. Kim, D. Kim and H. Furuta, Synthesis of a Black Dye with Absorption Capabilities Across the Visible-to-Near-Infrared Region: A MO-Mixing Approach via Heterometal Coordination of Expanded Porphyrinoid, *J. Am. Chem. Soc.*, 2020, **142**, 6807–6813.
8 Y. Wang, K. Ogasahara, D. Tomihama, R. Mysliborski, M. Ishida, Y. Hong, Y. Notsuka, Y. Yamaoka, T. Murayama, A. Muranaka, M. Uchiyama, S. Mori, Y. Yasutake, S. Fukatsu, D. Kim and H. Furuta, Near-Infrared-III-

Absorbing and -Emitting Dyes: Energy-Gap Engineering of Expanded Porphyrinoids via Metallation, *Angew. Chem., Int. Ed.*, 2020, **59**, 16161–16166.

9 T. Higashino, Y. Kurumisawa, S. Nimura, H. Iiyama and H. Imahori, Enhanced Donor–π–Acceptor Character of a Porphyrin Dye Incorporating Naphthobisthiadiazole for Efficient Near-Infrared Light Absorption, *Eur. J. Org Chem.*, 2018, **2018**, 2537–2547.

10 H. Mori, T. Tanaka and A. Osuka, Fused porphyrinoids as promising near-infrared absorbing dyes, *J. Mater. Chem. C*, 2013, **1**, 2500–2519.

11 L. Edwards, M. Gouterman and C. B. Rose, Synthesis and vapor spectrum of zinc tetrabenzporphine, *J. Am. Chem. Soc.*, 1976, **98**, 7638–7641.

12 S. Ito, T. Murashima and N. Ono, A new synthesis of pyrroles fused with polycyclic skeletons, *J. Chem. Soc., Perkin Trans. 1*, 1997, 3161–3166.

13 C. M. B. Carvalho, T. J. Brocksom and K. T. de Oliveira, Tetrabenzoporphyrins: synthetic developments and applications, *Chem. Soc. Rev.*, 2013, **42**, 3302–3317.

14 S. Ito, N. Ochi, H. Uno, T. Murashima and N. Ono, A new synthesis of [2,3]naphthoporphyrins, *Chem. Commun.*, 2000, 893–894.

15 O. S. Finikova, A. V. Cheprakov and S. A. Vinogradov, Synthesis and Luminescence of Soluble Meso-Unsubstituted Tetrabenzo- and Tetranaphtho[2,3] porphyrins, *J. Org. Chem.*, 2005, **70**, 9562–9572.

16 T. Khoury and M. J. Crossley, A strategy for the stepwise ring annulation of all four pyrrolic rings of a porphyrin, *Chem. Commun.*, 2007, 4851–4853.

17 M. A. Filatov, S. Baluschev, I. Z. Ilieva, V. Enkelmann, T. Miteva, K. Landfester, S. E. Aleshchenkov and A. V. Cheprakov, Tetraaryltetraanthra[2,3]porphyrins: Synthesis, Structure, and Optical Properties, *J. Org. Chem.*, 2012, 77, 11119–11131.

18 V. Yakutkin, S. Aleshchenkov, S. Chernov, T. Miteva, G. Nelles, A. Cheprakov and S. Baluschev, Towards the IR Limit of the Triplet–Triplet Annihilation-Supported Up-Conversion: Tetraanthraporphyrin, *Chem.–Eur. J.*, 2008, **14**, 9846–9850.

19 F. Wu, Y. Sun, H. Gao, X. Zhi, Y. Zhao and Z. Shen, Boosting near-infrared photothermal/photoacoustic conversion performance of anthracene-fused porphyrin via paramagnetic ion coordination strategy, *Sci. China: Chem.*, 2023, **66**, 164–173.

20 Y. Fan, Z. Zeng, H. Shu, M. Zhou, L. Xu, Y. Rao, T. Gu, X. Liang, W. Zhu and J. Song, Two- and three-dimensional β,β′-N-heterocycle fused porphyrins: concise construction, singlet oxygen production and electro-catalytic hydrogen evolution reaction, *Org. Chem. Front.*, 2021, **8**, 6080–6088.

21 J. R. Sommer, A. H. Shelton, A. Parthasarathy, I. Ghiviriga, J. R. Reynolds and K. S. Schanze, Photophysical Properties of Near-Infrared Phosphorescent π-Extended Platinum Porphyrins, *Chem. Mater.*, 2011, **23**, 5296–5304.

22 H. Yamada, D. Kuzuhara, T. Takahashi, Y. Shimizu, K. Uota, T. Okujima, H. Uno and N. Ono, Synthesis and Characterization of Tetraanthroporphyrins, *Org. Lett.*, 2008, **10**, 2947–2950.

23 N. Kobayashi, T. Furuyama and K. Satoh, Rationally Designed Phthalocyanines Having Their Main Absorption Band beyond 1000 nm, *J. Am. Chem. Soc.*, 2011, **133**, 19642–19645.

24 T. Furuyama, K. Satoh, T. Kushiya and N. Kobayashi, Design, Synthesis, and Properties of Phthalocyanine Complexes with Main-Group Elements Showing Main Absorption and Fluorescence beyond 1000 nm, *J. Am. Chem. Soc.*, 2014, **136**, 765–776.

25 T. Hoshi and N. Kobayashi, Spectroscopic and structural properties of phthalocyanines deduced from their frontier molecular orbitals (MOs) and MO calculations, *Coord. Chem. Rev.*, 2017, **345**, 31–41.

26 H. L. Anderson, Meso-alkynyl porphyrins, *Tetrahedron Lett.*, 1992, **33**, 1101–1104.

27 T. Tanaka and A. Osuka, Conjugated porphyrin arrays: synthesis, properties and applications for functional materials, *Chem. Soc. Rev.*, 2015, **44**, 943–969.

28 M. D. Peeks, T. D. W. Claridge and H. L. Anderson, Aromatic and antiaromatic ring currents in a molecular nanoring, *Nature*, 2017, **541**, 200–203.

29 A. Summerfield, M. Baldoni, D. V. Kondratuk, H. L. Anderson, S. Whitelam, J. P. Garrahan, E. Besley and P. H. Beton, Ordering, flexibility and frustration in arrays of porphyrin nanorings, *Nat. Commun.*, 2019, **10**, 2932.

30 H. S. Jung, P. Verwilst, A. Sharma, J. Shin, J. L. Sessler and J. S. Kim, Organic molecule-based photothermal agents: an expanding photothermal therapy universe, *Chem. Soc. Rev.*, 2018, **47**, 2280–2297.

31 Y. Ishii, S. Ito, Y. Saito, D. Uno and T. Oba, Synthesis of [2,3] naphthoporphyrins using 4,9-dihydro-4,9-ethano-2*H*-benz[*f*] isoindole as a benz[*f*]isoindole equivalent, *Tetrahedron*, 2015, **71**, 8892–8898.

32 G. A. Brito, F. Della-Felice, G. Luo, A. S. Burns, R. A. Pilli, S. D. Rychnovsky and M. J. Krische, Catalytic Enantioselective Allylations of Acetylenic Aldehydes via 2-Propanol-Mediated Reductive Coupling, *Org. Lett.*, 2018, **20**, 4144–4147.

33 Y. Sun, F. Wu, H. Gao, C. Qu, K. Wang, Y. Zhao and Z. Shen, Ruffle-distorted meso-silylethynyl-substituted naphthoporphyrin showing near-infrared Q band beyond 800 nm, *J. Porphyrins Phthalocyanines*, 2023, **27**, 114–120.

34 S. Ito, T. Murashima, N. Ono and H. Uno, A new synthesis of benzoporphyrins using 4,7-dihydro-4,7-ethano-2*H*-isoindole as a synthon of isoindole, *Chem. Commun.*, 1998, 1661–1662.

35 J. E. Rogers, K. A. Nguyen, D. C. Hufnagle, D. G. McLean, W. Su, K. M. Gossett, A. R. Burke, S. A. Vinogradov, R. Pachter and P. A. Fleitz, Observation and Interpretation of Annulated Porphyrins: Studies on the Photophysical Properties of Meso-Tetraphenylmetalloporphyrins, *J. Phys. Chem. A*, 2003, **107**, 11331–11339.

36 T. Lu and F. Chen, Multiwfn: a multifunctional wavefunction analyzer, *J. Comput. Chem.*, 2012, **33**, 580–592.

37 S. Klod and E. Kleinpeter, Ab initio calculation of the anisotropy effect of multiple bonds and the ring current

effect of arenes-application in conformational and configurational analysis, *J. Chem. Soc., Perkin Trans. 2*, 2001, 1893–1898.

38 H. M. Marques and I. Cukrowski, Molecular mechanics parameters for the modelling of four-coordinate Zn(II) porphyrins, *Phys. Chem. Chem. Phys.*, 2003, **5**, 5499–5506.

39 A. Hazell, Structure of (5,10,15,20-tetraphenyl-21*H*,23*H*-porphinato)platinum(II), $C_{44}H_{28}N_4Pt$, *Acta Crystallogr., Sect. C: Struct. Chem.*, 1984, **40**, 751–753.

40 T. M. Krygowski, Crystallographic studies of inter-and intramolecular interactions reflected in aromatic character of pi-electron systems, *J. Chem. Inf. Comput. Sci.*, 1993, **33**, 70–78.

41 M. K. Cyrañski, T. M. Krygowski, M. Wisiorowski, N. J. R. van Eikema Hommes and P. v. R. Schleyer, Global and Local Aromaticity in Porphyrins: An Analysis Based on Molecular Geometries and Nucleus-Independent Chemical Shifts, *Angew. Chem., Int. Ed.*, 1998, **37**, 177–180.

42 W. Jentzen, X.-Z. Song and J. A. Shelnutt, Structural Characterization of Synthetic and Protein-Bound Porphyrins in Terms of the Lowest-Frequency Normal Coordinates of the Macrocycle, *J. Phys. Chem. B*, 1997, **101**, 1684–1699.

43 C. J. Kingsbury and M. O. Senge, The shape of porphyrins, *Coord. Chem. Rev.*, 2021, **431**, 213760.

44 J. Mack, M. J. Stillman and N. Kobayashi, Application of MCD spectroscopy to porphyrinoids, *Coord. Chem. Rev.*, 2007, **251**, 429–453.

45 J. Mack, Y. Asano, N. Kobayashi and M. J. Stillman, Application of MCD Spectroscopy and TD-DFT to a Highly Non-Planar Porphyrinoid Ring System. New Insights on Red-Shifted Porphyrinoid Spectral Bands, *J. Am. Chem. Soc.*, 2005, **127**, 17697–17711.

46 W. Zhang, S. Chen, P. Sun, S. Ye, Q. Fan, J. Song, P. Zeng, J. Qu and W.-Y. Wong, NIR-II J-Aggregated Pt(II)-Porphyrin-Based Phosphorescent Probe for Tumor-Hypoxia Imaging, *Adv. Healthcare Mater.*, 2022, **11**, 2200467.

47 S. Kumar, Y. K. Maurya, T. Lis and M. Stępień, Synthesis of a donor–acceptor heterodimer via trifunctional completive self-sorting, *Nat. Commun.*, 2022, **13**, 3204.

48 B. Golec, J. Buczyńska, K. Nawara, A. Gorski and J. Waluk, Photodegradation of free base and zinc porphyrins in the presence and absence of oxygen, *Photochem. Photobiol. Sci.*, 2023, **22**, 2725–2734.

49 Z. Zhou, X. Zhou, Q. Liu, X. Zhang and H. Liu, Fixation of Zinc(II) Ion to Dioxygen in a Highly Deformed Porphyrin: Implications for the Oxygen Carrier Mechanism of Distorted Heme, *Org. Lett.*, 2015, **17**, 4078–4081.

50 F. Rusydi, M. Kemal Agusta, A. Gandaryus Saputro and H. Kasai, A First Principles Study on Zinc–Porphyrin Interaction with O_2 in Zinc–Porphyrin(Oxygen) Complex, *J. Phys. Soc. Jpn.*, 2012, **81**, 124301.

51 J. Yang, Y. Zhang, X. Wu, W. Dai, D. Chen, J. Shi, B. Tong, Q. Peng, H. Xie, Z. Cai, Y. Dong and X. Zhang, Rational design of pyrrole derivatives with aggregation-induced phosphorescence characteristics for time-resolved and two-photon luminescence imaging, *Nat. Commun.*, 2021, **12**, 4883.

52 Z. Chen, C. S. Wannere, C. Corminboeuf, R. Puchta and P. v. R. Schleyer, Nucleus-Independent Chemical Shifts (NICS) as an Aromaticity Criterion, *Chem. Rev.*, 2005, **105**, 3842–3888.

53 D. Geuenich, K. Hess, F. Köhler and R. Herges, Anisotropy of the Induced Current Density (ACID), a General Method to Quantify and Visualize Electronic Delocalization, *Chem. Rev.*, 2005, **105**, 3758–3772.

54 H. Fliegl, S. Taubert, O. Lehtonen and D. Sundholm, The gauge including magnetically induced current method, *Phys. Chem. Chem. Phys.*, 2011, **13**, 20500–20518.

55 H. Fliegl, J. Jusélius and D. Sundholm, Gauge-Origin Independent Calculations of the Anisotropy of the Magnetically Induced Current Densities, *J. Phys. Chem. A*, 2016, **120**, 5658–5664.